Identification and validation of constitutive parameters of a Hencky-type discrete model via experiments on millimetric pantographic unit cells

Michele De Angelo, Nurettin Yilmaz, M. Erden Yildizdag, Anil Misra, François Hild, Francesco Dell'isola

To cite this version:

Michele De Angelo, Nurettin Yilmaz, M. Erden Yildizdag, Anil Misra, François Hild, et al.. Identification and validation of constitutive parameters of a Hencky-type discrete model via experiments on millimetric pantographic unit cells. International Journal of Non-Linear Mechanics, 2023, pp.104419. 10.1016/j.ijnonlinmec.2023.104419 . hal-04079561

HAL Id: hal-04079561
https://hal.science/hal-04079561v1

Identification and validation of constitutive parameters of a Hencky-type discrete model via experiments on millimetric pantographic unit cells

Michele De Angelo[a,b], Nurettin Yilmaz[c], M. Erden Yildizdag[c,d,*], Anil Misra[b], François Hild[e], Francesco dell'Isola[a,c]

[a] *Dipartimento di Ingegneria Civile, Edile-Architettura e Ambientale, Universita degli Studi dell'Aquila, Via Giovanni Gronchi 18 - Zona Industriale di Pile, 67100 L'Aquila, Italy*
[b] *Civil, Environmental and Architectural Engineering Department, University of Kansas, 1530W 15th Street, Learned Hall, Lawrence, KS 66045-7609, USA*
[c] *International Research Center on Mathematics and Mechanics of Complex Systems, University of L'Aquila, L'Aquila, Italy*
[d] *Faculty of Naval Architecture and Ocean Engineering, Istanbul Technical University, 34469 Istanbul, Turkey*
[e] *Université Paris-Saclay, CentraleSupélec, ENS Paris-Saclay, CNRS, LMPS - Laboratoire de Mécanique Paris-Saclay, 91190 Gif-sur-Yvette, France*

Abstract

Pantographic metamaterial design benefits from model identification procedures starting from what can be considered as the elementary unit cell of larger pantographic structures. Results from a tensile experiment and digital image correlation are utilized to identify the constitutive parameters of a discrete Hencky-type model for a millimetric pantographic cell. In the performed calibration, two different cost functions are formulated. First, the cost function is based upon measured resultant forces on the specimen boundaries. Then, the second cost function is based upon the measured pivot displacements in addition to reaction forces. The second cost functions thus exploits the pivot kinematics, which is a key feature of the deformation of pantographic structures. The identified model is further validated by predicting the reaction forces and pivot displacements of the same specimen subjected to compression. It is shown that the identification with the cost function incorporating pivot displacements is superior. It is also noted that the calibrated parameters deviate considerably from their initial guess derived from the linear Saint Venant problem, thereby indicating microscale nonlinear affects in otherwise linear reaction force-precribed displacement responses at the macroscale.

Keywords: pantographic structures; digital image correlation; discrete model; inverse analysis

2010 MSC: 00-01, 99-00

---

[*] Corresponding author
Email address: `yildizdag@itu.edu.tr` (M. Erden Yildizdag)

---

1 Introduction

Recently developed technologies, such as additive manufacturing and powerful computing hardware, allow objects with many shapes and constituent materials to be designed, and their behavior to be analyzed with advanced numerical tools. These aspects are of fundamental importance in continuum mechanics research, especially in the field of metamaterials, which focuses on materials (usually manufactured with 3D printing techniques) exhibiting unusual macroscopic properties for designed mesostructures. In this context, pantographic metamaterials have recently been investigated because they possess interesting theoretical, mechanical, manufacturing, and experimental peculiarities [1, 2, 3]. A key property observed during experiments is their elastic elongation regime that may become very large when compared to standard materials [4, 5]. Moreover, unlimited possibilities seem to be open in the fabrication of lower-scale mesostructures for materials to be used at larger scales [6].

From a theoretical perspective, the research on pantographic metamaterials originated from the purpose of creating and developing mesostructured architectures whose strain energy functional substantially depended on the second gradients of the displacement field [7, 8, 9, 10, 11]. Classical continuum mechanics is not appropriate to describe structured media, unless one develops a model that is extremely faithful to the chosen topology, and solves algebraic systems running into excessively long computation time. Consequently, there is a need for developing higher gradient or higher-order models [12, 13, 14, 15]. An example that deals with using a wider kinematic basis rather than higher gradients of the same placement field are granular metamaterials and granular micromechanics [16, 17, 18, 19]. The crucial point is to conjecture the right mathematical model that is faithful to a certain degree of the physical system under consideration and allows for the evaluation up to a pre-established accuracy of some aspects of interest. For pantographic (i.e., mesostructured) materials, the following three approaches have been developed for describing their mechanical behavior [20, 21, 22], each having its limitations and strengths:

- continuum approach [23, 24, 25, 26];
- discrete approach [27, 28, 29];

- experimental approaches using the potentialities of 3D printing processes [30, 31, 32, 33].

Common to both continuum and discrete descriptors, there is a need for estimating the constitutive parameters. Recent studies revealed a rather satisfactory agreement between theoretical predictions and actual experimental evidence [34, 35, 36, 37, 38, 39, 40, 41]. Additionally, the strong connection between discrete and continuous constitutive parameters must be noted when a macromodel, which is meant as a generalized 2D continuum [42, 43], is deduced by heuristic identification from a discrete model that provides detailed descriptions of the deformation mechanisms of the mesostructure [23] (for more details about identification procedures see Refs. [44, 45, 46, 47, 48, 49, 50, 51]).

There have been few attempts relative to the links between constitutive parameters for continuum and discrete models, or vice versa, and a satisfactory answer to the following questions is still missing: how can constitutive parameters be estimated for a continuum or discrete model starting from the results of experiments? What are the relationships between the constitutive parameters for continuum and discrete models? The present work is a first attempt to partly address these questions.

The study of pantographic metamaterials requires identifying each of its elementary component properties to optimize particular application performances. The overall properties of any considered metamaterial depend on their morphology and the mechanical properties of their elementary constituents [52, 53]. The calibration procedure depends upon the development of an efficient conceptual framework that integrates all relevant design steps, thereby creating a collaborative feedback loop between different techniques. In particular, the measurement of kinematic data in addition to applied forces is very important. Among many different techniques, Digital Image Correlation (DIC) plays a prominent role [54, 55, 56] to create the envisioned synergistic approach. DIC is an (automatated) image analysis method that measures deformation fields and generates displacement and strain fields at prescribed resolution. In this non-contacting technique, mathematical/numerical registration procedures are used to process digital images of specimens recorded during experiments. Refined and detailed measurements of material deformations are essential to guide the synthesis process and to validate its results. The DIC techniques have proven to be effective in analyzing experimental results, and they can provide a rapid feedback to guide numerical and theoretical applications in metamaterial design [2, 3, 57]. Further, DIC techniques are also capable of measuring displacement fields at different length scales [58, 2, 3, 59, 60].

In the following, parameter identification of a discrete Hencky-type model for a millimetric pantographic unit cell is conducted. The procedure consists in using different types of objective functions that contain data of different nature. To be specific, reaction force data of mechanical tests on millimetric pantographic unit cells were employed along with displacements measured via DIC. The rationale of the investigation is to develop an identification procedure in the field of pantographic metamaterials starting from what can be considered as the elementary unit of larger pantographic structures. The content of this paper is organized as follows. Section 2 provides a definition for a Hencky-type discrete model of a pantographic unit cell. Section 3 provides information about a specimen of millimetric pantograph and the process of 3D printing. Section 4 includes the application of microscopic DIC analyses. Section 5 introduces the method of inverse analysis for parameter identification. Section 6 is devoted to the representation of the results for validation purposes with the predicted compressive behavior.

2 Hencky-type discrete model of pantographic unit cell

Generally, a pantographic sheet is considered as a rectangular lattice made of square cells. The cells, whose side length is ε, are formed by two orthogonal arrays of fibers. Arrays 1 and 2 are forming $\pi/4$ and $-\pi/4$ angles with respect to the (horizontal) x_1 axis (see Figure 1), respectively.

The discrete Lagrangian system, which is introduced to describe the pantographic unit cell, is made up of a finite number N of material particles occupying the intersection points of the two arrays of beams. These particles are linked to one another by means of extensional and rotational springs, whose arrangement is sketched in Figure 1. It is worth noting that this arrangement allows for both pair-wise and triple-particle interactions. With respect to the reference configuration, the position of the i^{th} particle is indicated by vector $\mathbf{P}_i$. The Lagrangian coordinates of this system are the positions of the particles after deformation, which are denoted with lowercase letters $\mathbf{p}_i$. If the kinematics of the system is limited to planar motions, one just needs to introduce $2N$ Lagrangian coordinates to describe the whole system. Once the kinematics of system has been defined, Lagrangian functions are to be derived for this mechanical system such that, by requiring the first variation of the associated functional to vanish, one obtains the equilibrium configurations

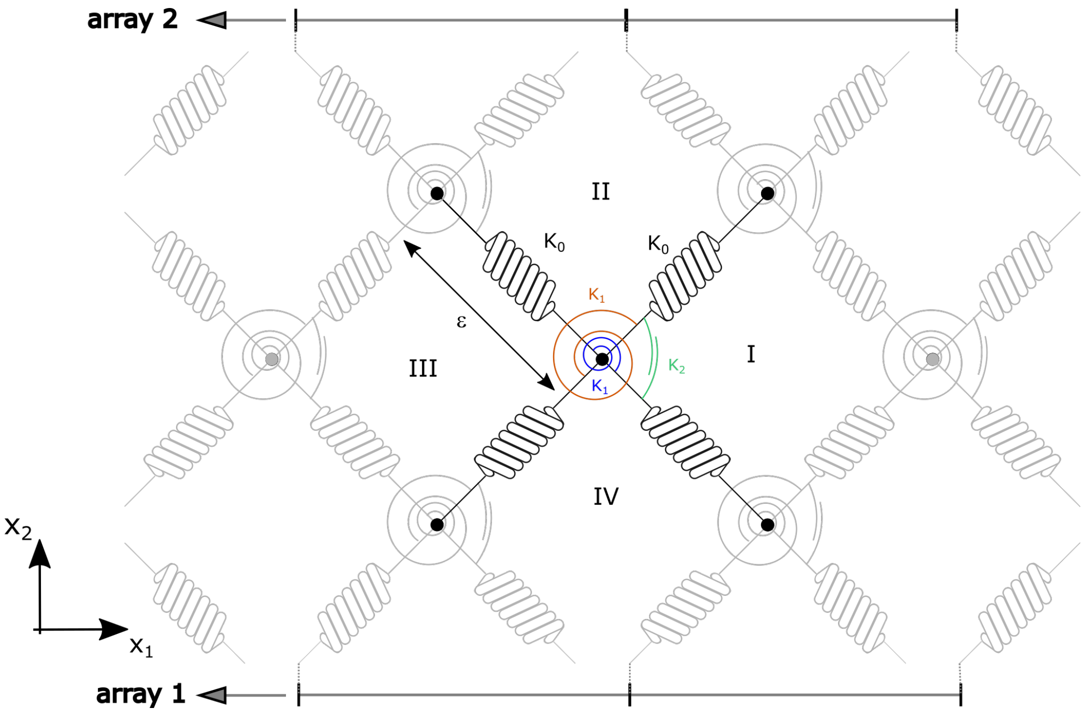

Figure 1: Discrete Hencky-type mechanical model for the pantographic lattice.

of the system. Since equilibrium configurations are sought, the Lagrangian function will only contain the potential energy part (i.e. the contribution associated with the relevant deformation).

Every pantographic substructure considered hereafter mainly undergoes three deformation modes (see Figure 2):

- extension of every beam segment of the fibres
- flexure of beam segments
- microtorsion of interconnecting hinges.

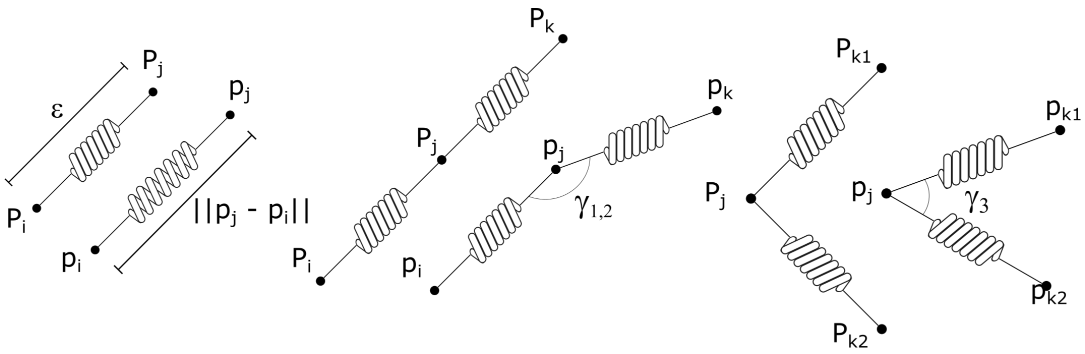

Figure 2: Extensional, flexural and shear spring kinematics.

Let us consider the discrete system depicted in Figure 3, which accounts for 11 hinges. The total energy of the pantographic sheet is expressed as

$$\mathcal{W}(\mathbf{d}) = \mathcal{W}_{int} - \mathcal{L}_{ext} = \sum_e (w_0 + w_1 + w_2) - \mathcal{L}_{ext} \tag{1}$$

where $\mathbf{d}$ is the vector collecting all the particle displacements, e an index labeling the springs of the system (Figures 2 and 3), $\mathcal{L}_{ext}$ the work done by external loads and

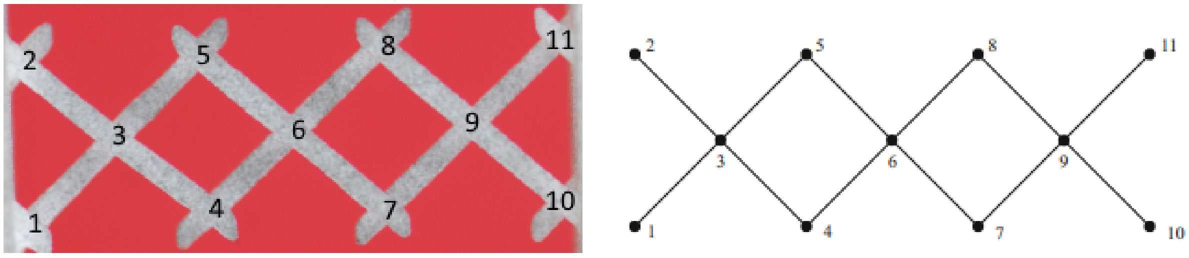

(a)

(b)

Figure 3: (a) Planar pantographic sheet highlighting hinges. (b) Corresponding sketch of pantographic structure.

- w_0 is the strain energy for axial springs

  $$w_0 = \frac{1}{2} K_0 \left(\|\mathbf{p}_j - \mathbf{p}_i\| - \varepsilon \right)^2 \tag{2}$$

  where $\mathbf{p}_i$ and $\mathbf{p}_j$ are the current positions of particles i and j, respectively, and K_0 the stiffness of the extensional spring;

- $w_{1,2}$ are the strain energies for flexural springs along arrays 1 and 2, respectively

  $$w_1 = K_1 \left(\cos \gamma_{1,2} + 1 \right) \tag{3}$$

  where angle γ_1 is written in terms of the Lagrangian coordinates as

  $$\cos \gamma_1 = \frac{\|\mathbf{p}_{j_{1,2}} - \mathbf{p}_{i_{1,2}}\|^2 + \|\mathbf{p}_{k_{1,2}} - \mathbf{p}_{j_{1,2}}\|^2 - \|\mathbf{p}_{k_{1,2}} - \mathbf{p}_{i_{1,2}}\|^2}{2\|\mathbf{p}_{j_{1,2}} - \mathbf{p}_{i_{1,2}}\| \|\mathbf{p}_{k_{1,2}} - \mathbf{p}_{j_{1,2}}\|} \tag{4}$$

  K_1 the stiffness of the rotational springs involving arrays 1 and 2, assumed equal for both arrays, $\mathbf{p}_{i_{1,2}}$, $\mathbf{p}_{j_{1,2}}$, and $\mathbf{p}_{k_{1,2}}$ the current positions of three particles aligned along arrays 1 or 2;

- w_2 is the strain energy for shear springs

  $$w_2 = \frac{1}{2} K_2 \left(\gamma_3 - \frac{\pi}{2} \right)^2 \tag{5}$$

where

$$\cos\gamma_3 = \frac{\|\mathbf{p}_{j_1}-\mathbf{p}_{k_2}\|^2+\|\mathbf{p}_{k_1}-\mathbf{p}_{j_1}\|^2-\|\mathbf{p}_{k_1}-\mathbf{p}_{k_2}\|^2}{2\|\mathbf{p}_{j_1}-\mathbf{p}_{k_2}\|\|\mathbf{p}_{k_1}-\mathbf{p}_{j_1}\|} \tag{6}$$

and K_2 the rigidity of the rotational springs that connect the two arrays, $\mathbf{p}_{k_1}$, $\mathbf{p}_{k_2}$, and $\mathbf{p}_{j_1}$ the Lagrangian coordinates of the involved particles. One such shear spring will appear in all the quadrants of Figure 1.

The solution to the equilibrium equations is achieved by means of a Matlab code, which implements an arc-length solution scheme [61].

3 Experiments

The structure under consideration is a millimetric pantograph shown in Figure 3 whose geometrical features are depicted in Figure 4. Different configurations were tested and the data obtained were used for both identification and validation procedures. The numerical values of the parameters for the specimen are given and labeled in Table 1. In the following, the labels of Table 1 are used to refer to the geometric configuration.

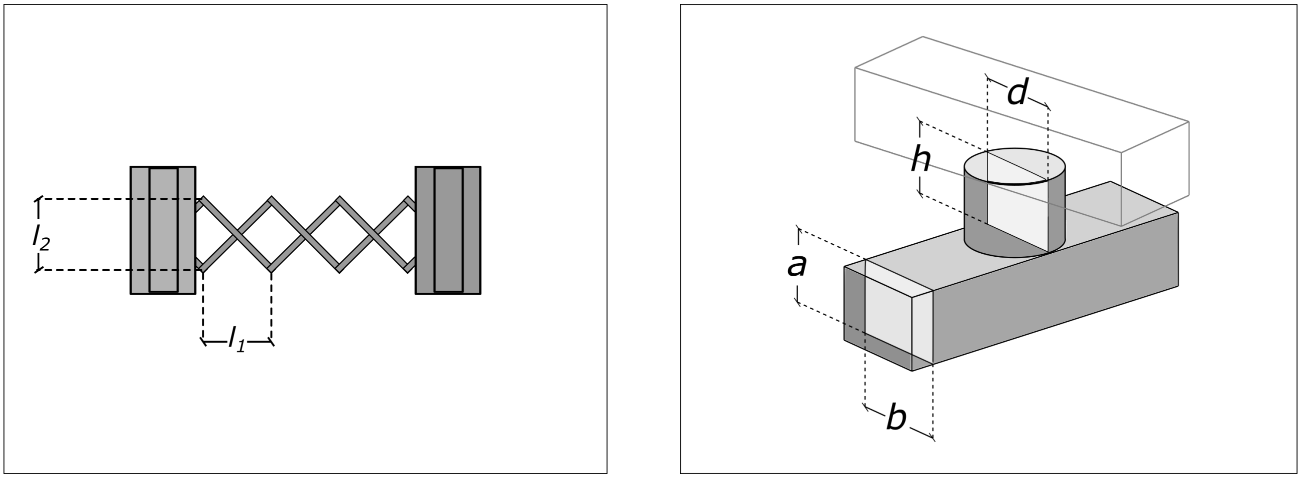

Figure 4: Parameters defining the pantographic unit cell.

Table 1: Geometrical parameters (expressed in mm) of the specimen tested for the inverse procedure.

ℓ_1	ℓ_2	a	b	d	h
8	8	1	1	1	3

The geometry of the metamaterial was initially generated with the CAD software SolidWorks (Dassault System SolidWroks Corporation, Waltham, MA, USA). The specimens were fabricated using a 3D printer Formiga P 100 (EOS GmbH, Munich, Germany) at the University of Technology, Warsaw, Poland. The 3D printer used a selective laser sintering (SLS) technology to produce the pantographic cells out of polyamide powder (PA2200), whose average grain size was 56 μm.

Two different tests, namely tensile and compressive, were performed on specimens having the geometry shown in Figure 4. The tensile test was experimentally carried out by keeping fixed one side of the specimen and applying an axial displacement on the other side. The maximum value of the prescribed displacement was ± 6 mm (with the convention that positive sign means extension of the specimen), at a rate of 0.1 mm/s.

A *Bose ElectroForce 3200* testing-device controlled by the software WinTest Material Testing System was used to perform all the experiments reported herein. The load cell used to measure the reaction force had a range of ±22 N, a measurement uncertainty of 0.1%. The studied pantographic metamaterial displayed a viscoelastic behavior. Therefore, the measured force-displacement curves are specific to a loading rate of 0.1 mm/s. The built-in transducer measuring the prescribed displacement has a range of ±6.5 mm, a measurement uncertainty of 0.1%. Pictures were acquired at a rate of 1/3 fps during each experiment. To improve the sensitivity of the correlation analysis, a mate black speckle pattern was spray-painted upon the surface of the sample. Figure 5 shows some cropped gray level pictures of the reference and deformed configurations of the tensile and compressive tests. Details on the equipment employed for image acquisition are provided in Table 2.

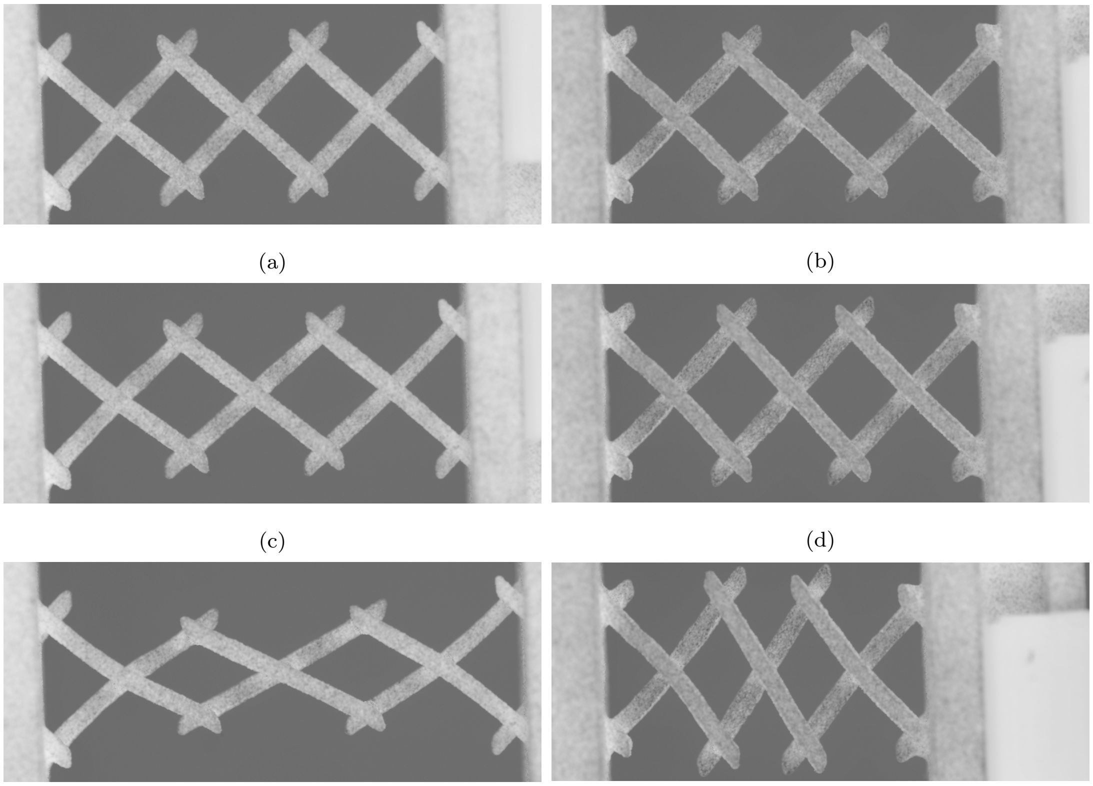

(a) (b)

(c) (d)

(e) (f)

Figure 5: Cropped gray level images of tensile (left) and compressive (right) tests. (a,b) Reference configurations, (c,d) 2.1 mm stroke, and (e,f) 6 mm stroke.

Table 2: DIC hardware parameters

Camera	NIKON D300
Definition	4288×2848 pixels (RGB image)
Gray Levels amplitude	8 bits
Lens	AF-S VR Micro-Nikkor 105mm f/2.8G ED
Aperture	$f/4.5$
Field of view	74×111 mm^2
Image scale	14.3 μm/px (B&W image)
Stand-off distance	≈ 40 cm
Image acquisition rate	1/3 fps
Exposure time	20 ms
Patterning technique	Sprayed black paint

4 Microscopic DIC analysis

Digital Image Correlation (DIC) is used to measure displacement fields at prescribed resolution of deformed specimens. The surface of the specimen has generally to be first prepared to make the motion of material hinges distinguishable by DIC [59]. During the experiments, digital images were recorded. At the beginning of the experiment, reference images were acquired to evaluate measurement uncertainties, and then the displacement field is measured with a correlation between the reference image and subsequent ones (of the deformed configuration). Recently, this technique has been applied to extract displacement fields of pantographic metamaterials [58, 59]. For pantographic metamaterials, FE-based DIC can be performed at least for three different length scale [59]. These displacement fields can then be compared with those predicted via numerical simulations, and, eventually, to calibrate and validate the considered constitutive model.

4.1 Global DIC

The registration of two gray level images in the reference (f) and deformed (g) configurations is based on the conservation of gray levels

$$f(\mathbf{x}) = g(\mathbf{x} + \mathbf{u}(\mathbf{x})) \tag{7}$$

where $\mathbf{u}$ is the (unknown) displacement field to be measured, and $\mathbf{x}$ the position of pixels. The sought displacement field minimizes the sum of squared differences Φ_C^2 over the region of interest (ROI)

$$\Phi_c^2 = \sum_{ROI} \phi_c^2(\mathbf{x}) \tag{8}$$

where ϕ_C defines the gray level residuals $\phi_c(\mathbf{x}) = f(\mathbf{x}) - g(\mathbf{x} + \mathbf{u}(\mathbf{x}))$ that are computed at each pixel position $\{\mathbf{x}\}$ of the ROI. The displacement field is expressed over a chosen kinematic basis

$$\mathbf{u}(\mathbf{x}) = \sum_{n} u_n \boldsymbol{\psi}_n(\mathbf{x}) \tag{9}$$

where $\boldsymbol{\psi}_n$ are vector fields and u_n the associated degrees of freedom, which are gathered in the column vector $\{\mathbf{u}\}$. Thus the measurement problem consists in the minimization of Φ_c^2 with respect to the unknown vector $\{\mathbf{u}\}$.

This problem is nonlinear and to obtain a solution a Gauss-Newton iterative scheme was implemented. In the following analyses, the vector fields correspond to the shape functions of 3-noded triangular elements (i.e., T3 elements). Consequently, the unknown degrees of freedom are the nodal displacements of the T3 elements.

4.2 Regularized DIC

The previous approach can be penalized when, for instance, the image contrast is not sufficient to achieve low spatial resolutions [59]. It consists in adding to the cost function Φ_c^2 penalty terms [62]. In the following, the penalty is based on the local equilibrium gap

$$\Phi_m^2 = \{\delta \mathbf{u}\}^\top [\mathbf{K}]^\top [\mathbf{K}] \{\delta \mathbf{u}\} \tag{10}$$

where $[\mathbf{K}]$ is the rectangular stiffness matrix restricted to the inner nodes and those associated with free edges [63], and $\{\delta \mathbf{u}\}$ the displacement increment between two analyzed images. Such type of regularization corresponds to the assumption of Hencky elasticity at the local level [59].

4.3 Hinge kinematics

In the present case, all beams were explicitly meshed (i.e., so-called microscopic DIC was carried out [59]). For the bottom layer, a mask was added for the overlapping zones close to the hinges. To be consistent with the selected model, the presence of the hinges between the two layers was accounted for through Lagrange multipliers, thereby enforcing no displacement jumps for each of them. These constraints lead to an additional penalty term.

The global residual to minimize consisted of the weighted sum of the previous two cost functions (i.e.,Φ_c^2 and Φ_m^2) and the augmentation. Because the dimensions of the first two cost functions is different, they need to be made dimensionless. The penalization weight acting on Φ_m^2 is proportional to a regularization length raised to the power 4 [63]. The larger the regularization length, the more weight is put on Φ_m^2. This penalization acts as a low-pass mechanical filter, namely, all high frequency components of the displacement field that are not mechanically admissible are filtered out. Similarly, for low-contrast areas mechanical regularization provides the displacement interpolation.

4.4 Registration quality

The root mean square (RMS) gray level residuals Φ_c of the DIC analyses of two tests are shown in Figure 6. Overall they remained very small in comparison to identical analyses [59]. Such observation proves that the measurements were trustworthy, and that the hypothesis of zero displacement jump at each hinge was consistent with the analyzed experiments.

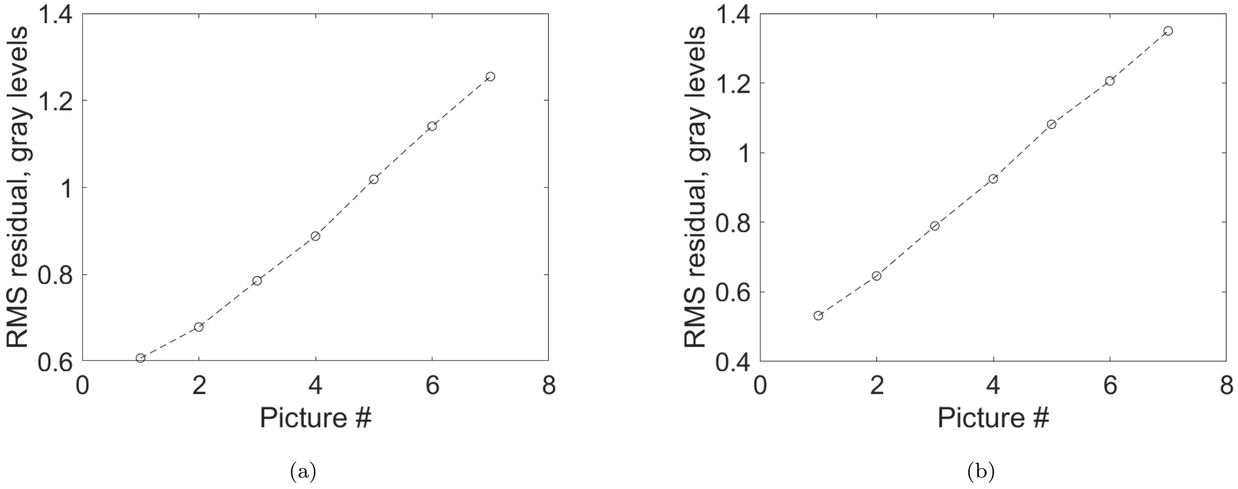

(a)

(b)

Figure 6: Gray level residuals of DIC analysis for the compressive (a) and tensile (b) tests.

5 Inverse analysis for parameter identification

The problem addressed herein is to determine:

- the elongation stiffness K_0 of each beam segment (characterized by the intersection points or location of the hinges) of the fibers
- the bending stiffness K_1 of beam segments,
- and the macroshear stiffness K_2 of interconnecting hinges (corresponding to micro-torsional stiffness).

The effort is directed toward obtaining the best stiffness set with a method that aggregates measurement results from difference sources into a single identification method while accounting for the uncertainty of each measurement. In this approach, the proper weighting of each contribution is important. In the following, the method employed is such that the weighting is not an arbitrary choice, but instead naturally follows from a Bayesian formulation given the number of measurements and their respective uncertainty. For the identification process at hand, the experimental data are the force measured by the load cell of the testing machine and the hinge displacements obtained from the recorded images of the sample surface.

Let us consider N observables, x_i with $i = 1, \ldots, N$, for which a model $\mathcal{G}_i(\mathbf{p})$ generates corresponding estimates from a set of m parameters $\{\mathbf{p}\} = \{\mathbf{p}_1, \mathbf{p}_2, \ldots, \mathbf{p}_m\}$ [64]

$$x_i = \mathcal{G}_i(\mathbf{p}) \tag{11}$$

Note that the observables x_i can be of different types with different units (e.g., a set of measured forces and displacements). The measurement $\hat{x}_i$ of the observable x_i is corrupted by Gaussian noise ζ_i

$$\hat{x}_i = x_i + \zeta_i \tag{12}$$

where a normal distribution, $\mathcal{N}(0, \sigma_i^2)$, for ζ_i with zero mean and variance σ_i^2 is assumed. Thus, the probability of the estimated observable to be equal to x_i for each measurement $\hat{x}_i$ reads

$$P_i = \frac{1}{(2\pi)^{1/2}\sigma_i} \exp\left(-\frac{(\hat{x}_i - x_i)^2}{2\sigma_i^2}\right), \tag{13}$$

Further, for the entire set of N measurements, assuming that they are statistically independent, the probability reads

$$P_i = \frac{1}{(2\pi)^{N/2}\prod_{i=1}^{N}\sigma_i} \exp\left(-\sum_{i=1}^{N}\frac{(\hat{x}_i - x_i)^2}{2\sigma_i^2}\right), \tag{14}$$

Inference of the most likely set of parameters that corresponds to a given set of measurements is equivalent to finding the maximum of Equation (14), or the minimum of the log-likelihood (up to irrelevant constants)

$$\chi^2(\{\mathbf{p}\}) = \frac{1}{N}\sum_{i=1}^{N}\frac{(\hat{x}_i - x_i)^2}{\sigma_i^2} \tag{15}$$

The choice of the prefactor is such that the expectation of χ^2 at convergence is 1, assuming that the difference $(\hat{x}_i - x_i)$ is only due to noise. It is also noteworthy that the quadratic difference is not any arbitrary choice among many convex functions that are minimum at the origin, but the consequence of the Gaussian probability density function assumed for noise. At this point, (possibly nonlinear) optimization methods are applied to find the optimal set of parameters that minimizes Equation (15).

The most important conclusion from Equation (15) is that an identification using different aggregated measurement sets (in the presence of white Gaussian noise) translates into minimizing the weighted sum of squared differences. Taking the example of two sets of measurement data, with N measurements and variances σ_1^2 and σ_2^2 respectively, and labeled sequentially from 1 to $N = N_1 + N_2$, the total cost function is decomposed as

$$(N_1 + N_2)\chi^2_{total}(\{\mathbf{p}\}) = \frac{1}{\sigma_1^2}\sum_{i=1}^{N_1}(\hat{x}_i - x_i(\{\mathbf{p}\}))^2 + \frac{1}{\sigma_2^2}\sum_{j=N_1+1}^{N}(\hat{x}_j - x_j(\{\mathbf{p}\}))^2 \tag{16}$$

In the present case, the measured data sets and the respective counterparts predicted by the model described above are (i) the reaction force set measured by the load cell, and (ii) the displacement component sets of the hinges.

The stiffness parameters necessary to completely describe the discrete model are K_0, K_1 and K_2. Thus, the parameter vector becomes

$$\{\mathbf{p}\} = \{K_0 \quad K_1 \quad K_2\}^\top \tag{17}$$

The identification was carried out by means of the following two different cost functions to observe the effect of including kinematic data in the identification process

$$\chi^2_F(\{\mathbf{p}\}) = \frac{\sum_n^N(\hat{F}_n - F_n(\{\mathbf{p}\}))^2}{\sigma_F^2} \tag{18}$$

$$\begin{aligned}\chi^2_{total}(\{\mathbf{p}\}) =& \frac{1}{\sigma_F^2}\sum_n^N(\hat{F}_n - F_n(\{\mathbf{p}\}))^2 + \\ & \frac{1}{R\sigma_u^2}\sum_i^R\sum_m^M(\hat{u}_{im} - u_{im}(\{\mathbf{p}\}))^2 + \\ & \frac{1}{R\sigma_v^2}\sum_i^R\sum_m^M(\hat{v}_{im} - v_{im}(\{\mathbf{p}\}))^2\end{aligned} \tag{19}$$

where $\hat{F}_n$ and $F_n(\{\mathbf{p}\})$ are measured and simulated reaction forces at time step n, N the total number of time steps of force measurements, and σ_F the standard force uncertainty. Further, $\hat{u}_{im}$ and $u_{im}(\{\mathbf{p}\})$ are the measured and simulated values of the displacement component parallel to the load application direction, while $\hat{v}_{im}$ and $v_{im}(\{\mathbf{p}\})$ are measured and simulated transverse displacement components for the $i-th$ hinge at time m. Parameter R denotes the total number of hinges (11 in this case), M the total number of images, and σ_u^2 and σ_v^2 are the variances of

Table 3: Standard force and displacement uncertainties.

σ_F(N)	σ_u and σ_v(px)
0.022	0.02

displacement uncertainties for the two directions, respectively. The standard uncertainties are given in Table 3.

The cost functions defined in Equations (18) and (19) are related to identification procedure 1 (or procedure 1) and identification procedure 2 (or procedure 2), respectively, in the remainder of this paper. From the viewpoint of model validity, it is noteworthy that the model parameters are properly estimated such that the cost functions are close to 1. The solution to the inverse problem defined by Equations (18) and (19) is obtained by iteratively minimizing the cost functions using a Gauss-Newton method starting with an initial guess for the parameters $\{K_0, K_1, K_2\}$. As a first estimate, the stiffnesses were obtained from the Saint-Venant problem (which is rigorously valid only for the linear case)

$$\begin{aligned} K_0 &= \frac{EA}{\ell} \\ K_1 &= \left(1 - \frac{\ell}{L}\right)\frac{EI}{\ell} \\ K_2 &= \frac{GI_p}{\ell_p} \end{aligned} \tag{20}$$

where E and G are the Young's and shear moduli of polyamide, respectively, A and I the area and inertia of the cross section, L the total length of the microbeams, and ℓ (i.e., $\frac{1}{2}\sqrt{\ell_1^2 + \ell_2^2}$) the distance between two neighboring hinges. The coefficient $1 - \ell/L$ takes into account the number of elastic hinges used to model the bending strain energy. The Young's modulus E and Poisson's ratio ν of polyamide [65] used in the 3D printing process are gathered in Table 4.

Table 4: Mechanical Properties of Polyamide PA 2200.

Young's modulus, E	Poisson's ratio, ν
1000 MPa	0.3

In Table 5, the first guess of the set of stiffnesses is reported along with the values obtained from identification procedures 1 and 2. It is notable that the axial stiffness K_0 and the torsional stiffness

K_2 identified using the two procedures are significantly smaller than their initial guess, which were estimated using linear approximation and ideal polyamide properties. In addition to the nonlinear effects, 3D printing of small objects may introduce defects that could result in considerably reducing the stiffness.

Table 5: Initial and calibrated stiffnesses by inverse analyses.

	K_0 (N/mm)	K_1 (Nmm)	K_2 (Nmm)
Initial set	280	12	20
Procedure 1	4	12	5.3
Procedure 2	18	8	2.1

The calibrated stiffness set is expected to reproduce the tensile experiment with good approximation. Figure 7 compares the reaction forces for the initial set of stiffnesses and at convergence of the two procedures. As the elastic regime was investigated, a limited range of data up to 2.1 mm of applied displacement was chosen. It is observed that the initial guess gives a considerably stiffer response and greatly overestimates the constitutive parameters. On the other hand both procedures 1 and 2 provide a significantly improved estimate of the measured load data. In particular the identified constitutive parameter K_0, related to beam extension, is found to be much smaller than that estimated using initial guess. It appears that the linear approximation of initial guess emphasises the role of the extension parameter. It is also possible that the printing defects alter the intrinsic properties of polyamide as well as the ideal behavior assumed in the initial guess. This last point is also reflected in the constitutive parameter K_2.

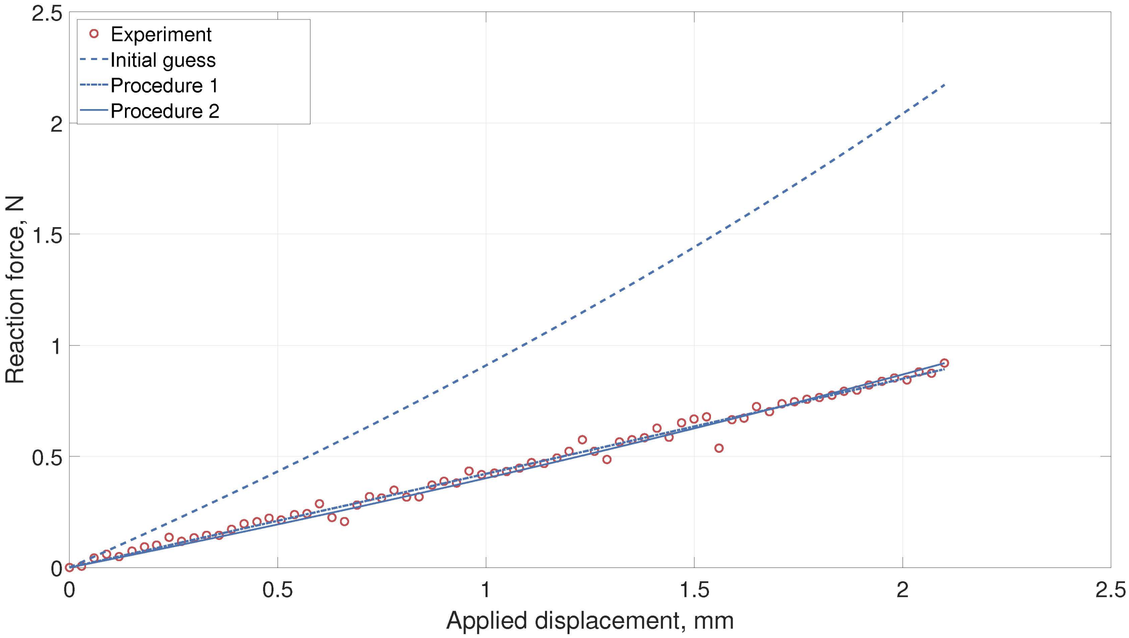

Figure 7: Tensile force vs. prescribed displacement associated with the initial set of stifnesses and those with the identification procedures 1 and 2.

To quantitatively compare the two identification procedures, Table 6 shows the normalized RMS errors of the calculated force (normalized by the uncertainty of the load cell). It is observed that the two sets of identified parameters, even if they differ in their numerical values (Table 5), resulted in good approximations of the measured reaction force. Procedure 1 led to slightly lower force residuals since it was the quantity that was minimized. Instead, in procedure 2 for which kinematic measurements were also included, the residuals are slightly higher. The fact that the two sets of parameters significantly changed shows that the inclusion of kinematic data enabled the model to be more faithful to the deformation and reaction force response of the specimen.

Table 6: χ_F cost functions related to the tensile test.

initial guess	procedure 1	procedure 2
30.5	1.1	1.2

Figure 8 shows the hinge displacement component parallel to the loading direction, indicated by the symbol u_x. Each graph refers to one hinge as labeled in Figure 3, and shows comparisons between experimental and simulated displacements corresponding to the stiffnesses reported in Table 5.

Differences between experiment and simulation are found for hinges 1 and 2. This observation shows that at those hinges the model predictions differed from the experimental results because the model boundary conditions assumed at the two hinges was not identical to those in the experiment. Alternatively, more realistic boundary conditions could be implemented in the numerical model by incorporating the connection between the actual boundary support and hinges 1 and 2. An excellent agreement is observed between experimental and numerical data on the displaced boundary, namely, at hinges 10 and 11, which provided evidence of the quality of the displacement measurements. For the internal hinges and both procedures, very small discrepancies are observed between the experimental and numerical data except for hinges 3, 4, and 5. Focusing on hinge 3, it is remarkable to discover that procedure 2 provided a better agreement. This outcome was due to having included the motion of the hinges within the calibration procedure.

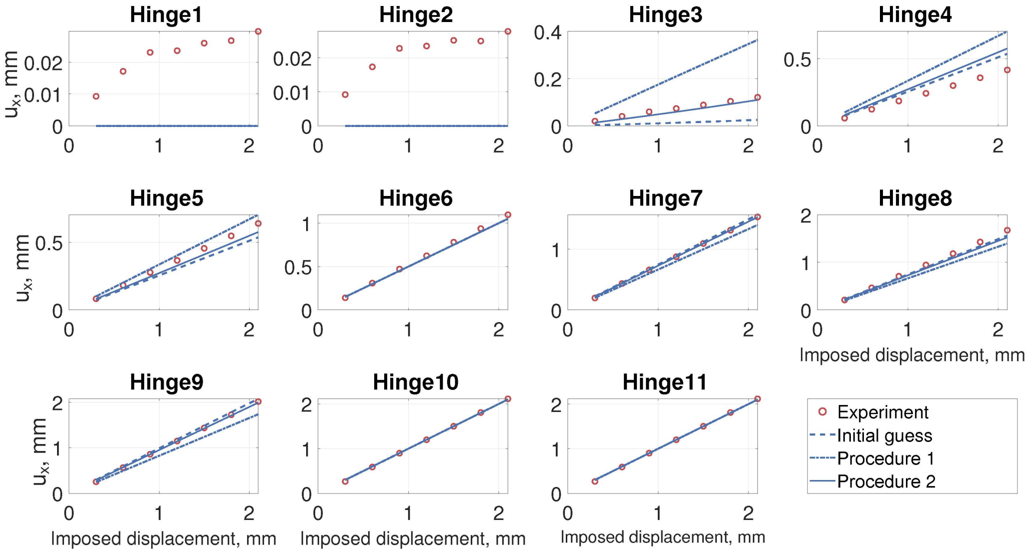

Figure 8: Longitudinal displacement component of the 11 hinges. Comparison between DIC measurements and simulations using the two sets of calibrated parameters.

A better appreciation of the previous effect is observed in Figure 9, which shows the hinge displacement component perpendicular to the loading direction, indicated by the symbol u_y. Apart from the boundary hinges where experimental fluctuations could not be captured by the model, in all other cases, the stiffness set derived via procedure 2 resulted in an improved correspondence between model and experiment.

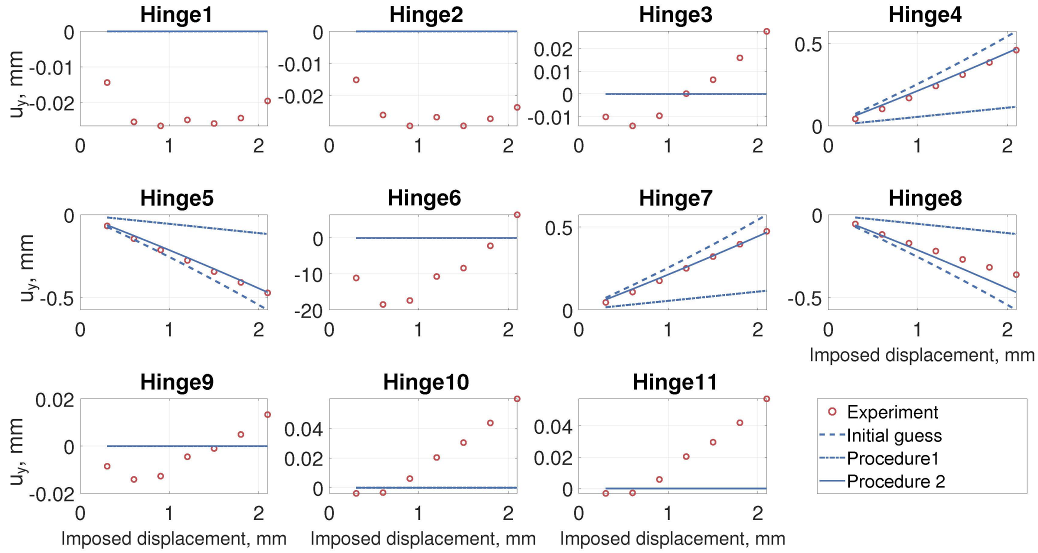

Figure 9: Transverse displacement component of the 11 hinges. Comparison between DIC measurements and simulations using the two sets of calibrated parameters.

The RMS differences of displacement components regarding each hinge are reported in Figure 10. The global RMS value is reported, which describes the overall quality of the displacement predictions. It is concluded that procedure 2 resulted in constitutive parameters that provided more reliable predictions (i.e., a factor two lower differences) of the hinge displacement displacement.

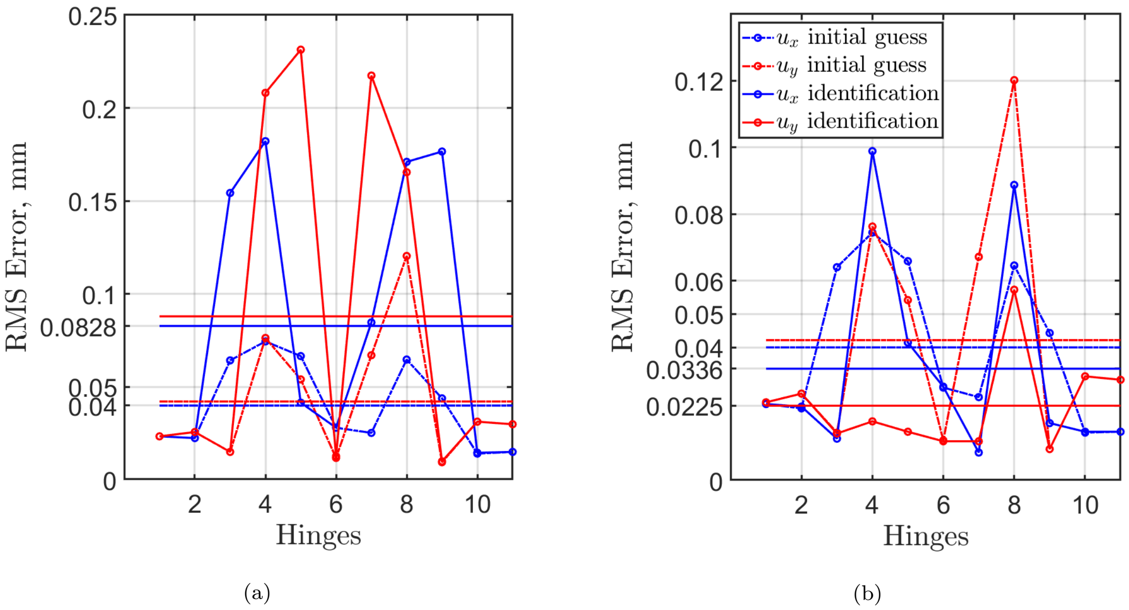

(a)

(b)

Figure 10: RMS displacement errors for each hinge of the tensile test. Comparison between experimental evidence and simulation with the calibrated parameters of procedures 1 (a) and 2 (b).

6 Validation with compressive test

It is desirable in material characterization that the calibrated parameters should allow satisfactory predictions for tests different from those used within the identification procedure. In the following, the results of a validation procedure are discussed in which the model prediction using the identified parameters (Table 5) are compared with experimental measurements for a compressive test. Figures 5 (b,d,f) show the reference and deformed configurations of the specimen under compressive loading. Important observations emerge when comparing experimental and predicted reaction forces in Figure 11. From a very discordant prediction with the initial guess, a significant improvement was obtained with the values calibrated with procedure 1, and an almost complete agreement occurred for procedure 2.

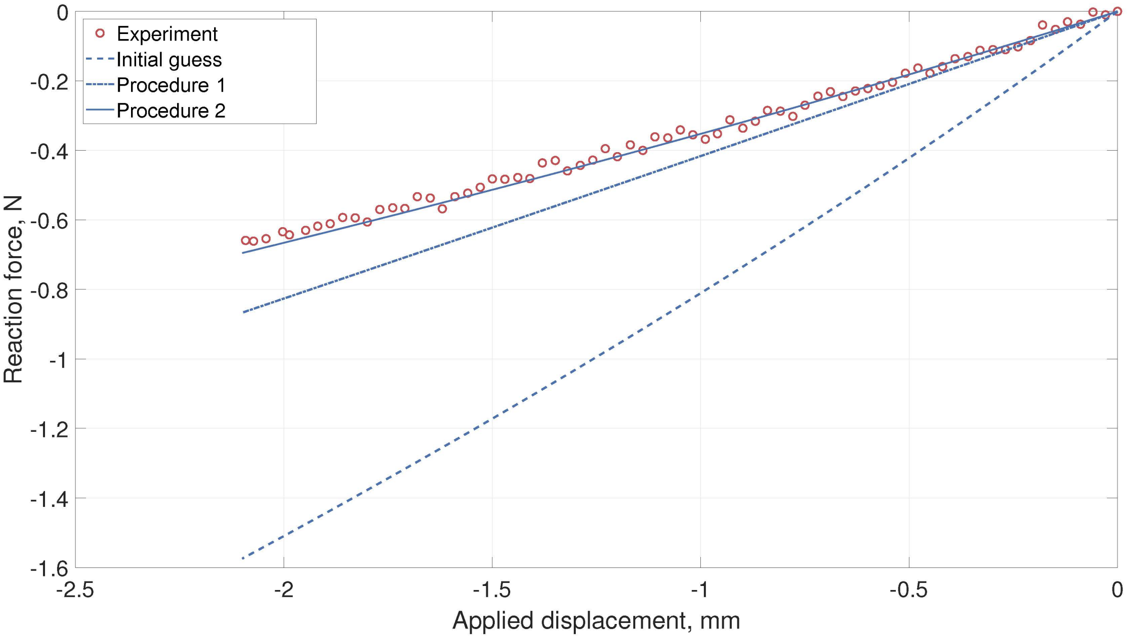

Figure 11: Compressive force vs. prescribed displacement associated the three parameters sets calibrated in tension.

Table 7 gathers the dimensionless force residuals for the predictions with the three sets of material parameters. In the present case, there is an even more pronounced difference between the two procedures, in favor of procedure 2, whose levels were very close to 1 (i.e., about five times lower than procedure 1).

Figures 12 and 13 show comparisons between the measured and predicted hinge motions. As for the tensile test, fluctuations in the hinges corresponding to the fixed side (i.e., 1 and 2), and a perfect

Table 7: χ_F cost functions related to compressive test.

Initial guess	Procedure 1	Procedure 2
24.7	4.7	0.9

interpolation for the displaced side (i.e., hinges 10 and 11) are noteworthy. Regarding the inner hinges, in most cases, there were no significant differences between the data. The set of stiffnesses provided by procedure 1, generally, led to larger discrepancies from the experiments than the initial guess. Figure 12 shows that hinge 3 was where marked differences occurred, which was also observed for the tensile test. The simulated displacement of hinge 3 exhibited a substantial deviation from real measurements for the initial guess and a marked improvement using the identified values.

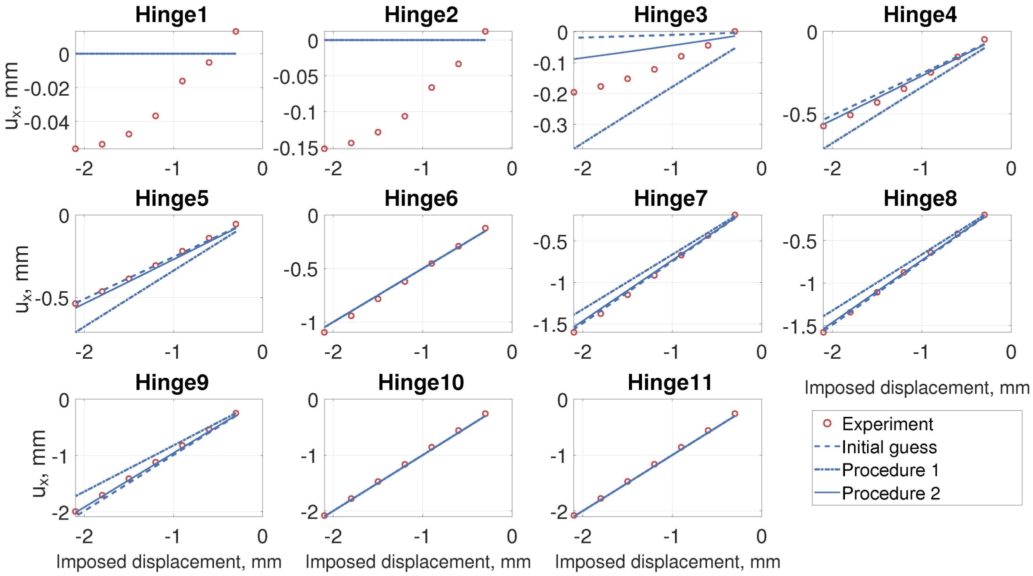

Figure 12: Longitudinal displacement component of the 11 hinges. Comparison between DIC measurements and predictions with the two sets of calibrated parameters.

When the results are further examined, it is confirmed that procedure 2 yielded better predictions than procedure 1. Similar observations apply for the transverse displacements in Figure 13.

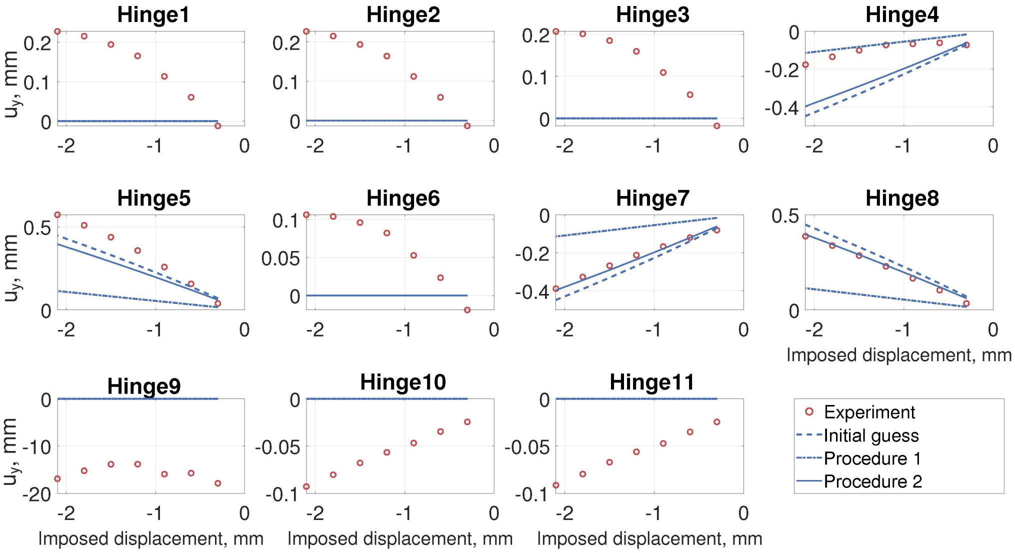

Figure 13: Transverse displacement component of the 11 hinges. Comparison between DIC measurements and predictions with the two sets of calibrated parameters.

Figure 14 confirms that procedure 1 produced an overall worsening on the predicted hinge displacements in both directions compared to the initial guess with procedure 2. An improvement in the RMS values is obtained.

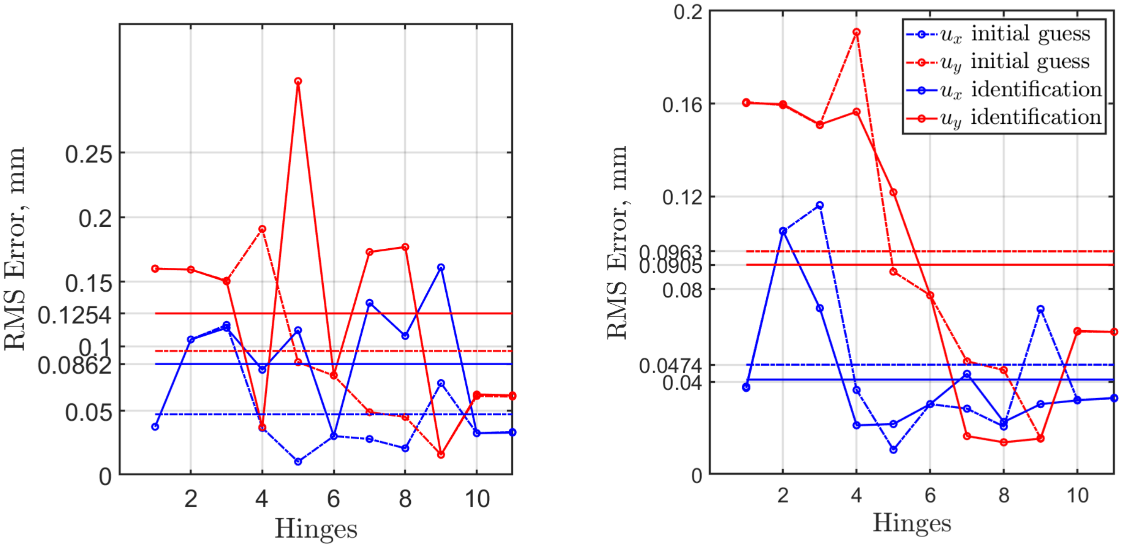

(a)

(b)

Figure 14: RMS displacement errors for each hinge of the compression test. Comparison between experimental evidence and predictions with the calibrated parameters of procedures 1 (a) and 2 (b).

7 Conclusion

In the present paper, the analysis of the deformation of millimetric pantographic unit cells was studied for model identification purposes using the measured results from a bias extension test. To this end, the measured deformation of the pantographic metamaterial was obtained using digital image correlation (DIC). Its behavior was modeled using a discrete Hencky-type framework. The identification of the constitutive parameters followed two different procedures. While the constitutive parameters were obtained by taking account of the reaction forces in both procedures 1 and 2, the measured displacements at the hinges in vertical and horizontal directions were also used in procedure 2. The RMS error of hinge displacement components were assessed. In addition, the efficiency of the two procedures was assessed in their ability to capture the force-displacement response. Procedure 2 was found to give closer agreement with the measurements.

The identified model was then applied to predict the response of the same specimen in compression. It was found that the identification carried out with procedure 2 resulted in more accurate predictions as compared to procedure 1. The introduction of kinematic data within the identification procedure resulted in a set of stiffnesses that was more consistent with the experimental evidence. This statement was true both regarding the tensile test that was used for calibration purposes, and the compressive test used for validation.

It should also be noted that the largest differences from the kinematic point of view occurred at hinges where the specimen failed in the tensile test (i.e., hinges 4 and 5). The latter observation suggests that the present model should include additional mechanisms that could have non-negligible effects. A hypothesis on the nature of these mechanisms could be linked to the particular geometry considered herein [34]. For pantographic structures having slender pivots, the flexibility of these structural elements is no longer negligible, and the strain energy density may also consider that zero displacement jump constrains between the two arrays of fibers does not hold [59]. In order to describe the kinematics of metamaterials with slender hinges, a modified version of the bi-dimensional model may be considered, which, in contrast to Ref. [23], takes into account relative displacements between the two families of fibers. It is believed that such enrichment of the kinematics to enclose these additional deformation mechanisms will lead to better results and identification performances.

References

[1] A. Misra, T. Lekszycki, I. Giorgio, G. Ganzosch, W. H. Müller, F. dell'Isola, Pantographic metamaterials show atypical poynting effect reversal, Mechanics Research Communications 89 (2018) 6–10.

[2] F. dell'Isola, P. Seppecher, M. Spagnuolo, E. Barchiesi, F. Hild, T. Lekszycki, I. Giorgio, L. Placidi, U. Andreaus, M. Cuomo, et al., Advances in pantographic structures: design, manufacturing, models, experiments and image analyses, Continuum Mechanics and Thermodynamics 31 (2019) 1231–1282.

[3] F. dell'Isola, P. Seppecher, J. J. Alibert, T. Lekszycki, R. Grygoruk, M. Pawlikowski, D. Steigmann, I. Giorgio, U. Andreaus, E. Turco, et al., Pantographic metamaterials: an example of mathematically driven design and of its technological challenges, Continuum Mechanics and Thermodynamics 31 (2019) 851–884.

[4] F. dell'Isola, T. Lekszycki, M. Pawlikowski, R. Grygoruk, L. Greco, Designing a light fabric metamaterial being highly macroscopically tough under directional extension: first experimental evidence, Zeitschrift für angewandte Mathematik und Physik 66 (2015) 3473–3498.

[5] M. De Angelo, M. Spagnuolo, F. D'annibale, A. Pfaff, K. Hoschke, A. Misra, C. Dupuy, P. Peyre, J. Dirrenberger, M. Pawlikowski, The macroscopic behavior of pantographic sheets depends mainly on their microstructure: experimental evidence and qualitative analysis of damage in metallic specimens, Continuum Mechanics and Thermodynamics 31 (2019) 1181–1203.

[6] Z. Vangelatos, M. E. Yildizdag, I. Giorgio, F. dell'Isola, C. Grigoropoulos, Investigating the mechanical response of microscale pantographic structures fabricated by multiphoton lithography, Extreme Mechanics Letters 43 (2021) 101202.

[7] J.-J. Alibert, P. Seppecher, F. dell'Isola, Truss modular beams with deformation energy depending on higher displacement gradients, Mathematics and Mechanics of Solids 8 (2003) 51–73.

[8] P. Seppecher, J.-J. Alibert, F. dell'Isola, Linear elastic trusses leading to continua with exotic mechanical interactions, in: Journal of Physics: Conference Series, volume 319, IOP Publishing, 2011, p. 012018.

[9] M. Cuomo, F. dell'Isola, L. Greco, N. Rizzi, First versus second gradient energies for planar sheets with two families of inextensible fibres: investigation on deformation boundary layers, discontinuities and geometrical instabilities, Composites Part B: Engineering 115 (2017) 423–448.

[10] F. dell'Isola, M. Cuomo, L. Greco, A. Della Corte, Bias extension test for pantographic sheets: numerical simulations based on second gradient shear energies, Journal of Engineering Mathematics 103 (2017) 127–157.

[11] N. Shekarchizadeh, M. Laudato, L. Manzari, B. E. Abali, I. Giorgio, A. M. Bersani, Parameter identification of a second-gradient model for the description of pantographic structures in dynamic regime, Zeitschrift für angewandte Mathematik und Physik 72 (2021) 1–24.

[12] R. D. Mindlin, Microstructure in linear elasticity, Technical Report, Columbia Univ New York Dept of Civil Engineering and Engineering Mechanics, 1963.

[13] R. D. Mindlin, Second gradient of strain and surface-tension in linear elasticity, International Journal of Solids and Structures 1 (1965) 417–438.

[14] P. Germain, The method of virtual power in continuum mechanics. Part 2: Microstructure, SIAM Journal on Applied Mathematics 25 (1973) 556–575.

[15] P. Germain, The method of virtual power in the mechanics of continuous media, i: Second-gradient theory, Mathematics and Mechanics of Complex Systems 8 (2020) 153–190.

[16] A. Misra, P. Poorsolhjouy, Grain-and macro-scale kinematics for granular micromechanics based small deformation micromorphic continuum model, Mechanics Research Communications 81 (2017) 1–6.

[17] I. Giorgio, M. De Angelo, E. Turco, A. Misra, A Biot–Cosserat two-dimensional elastic non-

linear model for a micromorphic medium, Continuum Mechanics and Thermodynamics (2019) 1–13.

[18] A. Misra, N. Nejadsadeghi, Longitudinal and transverse elastic waves in 1D granular materials modeled as micromorphic continua, Wave Motion 90 (2019) 175–195.

[19] N. Nejadsadeghi, A. Misra, Extended granular micromechanics approach: a micromorphic theory of degree n, Mathematics and Mechanics of Solids 25 (2020) 407–429.

[20] A. Ciallella, D. Pasquali, M. Gołaszewski, F. D'Annibale, I. Giorgio, A rate-independent internal friction to describe the hysteretic behavior of pantographic structures under cyclic loads, Mechanics Research Communications 116 (2021) 103761.

[21] M. Laudato, L. Manzari, I. Giorgio, M. Spagnuolo, P. Göransson, Dynamics of pantographic sheet around the clamping region: experimental and numerical analysis, Mathematics and Mechanics of Solids 26 (2021) 1515–1537.

[22] I. Giorgio, Lattice shells composed of two families of curved Kirchhoff rods: an archetypal example, topology optimization of a cycloidal metamaterial, Continuum Mechanics and Thermodynamics 33 (2021) 1063–1082.

[23] F. dell'Isola, I. Giorgio, M. Pawlikowski, N. L. Rizzi, Large deformations of planar extensible beams and pantographic lattices: heuristic homogenization, experimental and numerical examples of equilibrium, Proceedings of the Royal Society A: Mathematical, Physical and Engineering Sciences 472 (2016) 20150790.

[24] I. Giorgio, N. L. Rizzi, E. Turco, Continuum modelling of pantographic sheets for out-of-plane bifurcation and vibrational analysis, Proc. R. Soc. A 473 (2017) 20170636.

[25] E. Barchiesi, S. R. Eugster, L. Placidi, F. Dell'Isola, Pantographic beam: a complete second gradient 1D-continuum in plane, Zeitschrift für angewandte Mathematik und Physik 70 (2019) 1–24.

[26] I. Giorgio, N. L. Rizzi, U. Andreaus, D. J. Steigmann, A two-dimensional continuum model of

pantographic sheets moving in a 3D space and accounting for the offset and relative rotations of the fibers, Mathematics and Mechanics of Complex Systems 7 (2019) 311–325.

[27] E. Turco, F. dell'Isola, A. Cazzani, N. L. Rizzi, Hencky-type discrete model for pantographic structures: numerical comparison with second gradient continuum models, Zeitschrift für angewandte Mathematik und Physik 67 (2016) 85.

[28] E. Turco, I. Giorgio, A. Misra, F. dell'Isola, King post truss as a motif for internal structure of (meta) material with controlled elastic properties, Royal Society open science 4 (2017) 171153.

[29] E. Barchiesi, J. Harsch, G. Ganzosch, S. Eugster, Discrete versus homogenized continuum modeling in finite deformation bias extension test of bi-pantographic fabrics, Continuum Mechanics and Thermodynamics (2020) 1–14.

[30] M. Golaszewski, R. Grygoruk, I. Giorgio, M. Laudato, F. Di Cosmo, Metamaterials with relative displacements in their microstructure: technological challenges in 3D printing, experiments and numerical predictions, Continuum Mechanics and Thermodynamics 31 (2019) 1015–1034.

[31] G. Ganzosch, E. Barchiesi, R. Drobnicki, A. Pfaff, W. H. Müller, Experimental Investigations of 3D-Deformations in Additively Manufactured Pantographic Structures, in: International Summer School-Conference "Advanced Problems in Mechanics", Springer, 2019, pp. 101–114.

[32] E. Barchiesi, G. Ganzosch, C. Liebold, L. Placidi, R. Grygoruk, W. H. Müller, Out-of-plane buckling of pantographic fabrics in displacement-controlled shear tests: experimental results and model validation, Continuum Mechanics and Thermodynamics 31 (2019) 33–45.

[33] V. A. Eremeyev, E. Turco, Enriched buckling for beam-lattice metamaterials, Mechanics Research Communications 103 (2020) 103458.

[34] M. Spagnuolo, K. Barcz, A. Pfaff, F. dell'Isola, P. Franciosi, Qualitative pivot damage analysis in aluminum printed pantographic sheets: numerics and experiments, Mechanics Research Communications 83 (2017) 47–52.

[35] U. Andreaus, M. Spagnuolo, T. Lekszycki, S. R. Eugster, A Ritz approach for the static analysis

of planar pantographic structures modeled with nonlinear Euler–Bernoulli beams, Continuum Mechanics and Thermodynamics 30 (2018) 1103–1123.

[36] M. De Angelo, E. Barchiesi, I. Giorgio, B. E. Abali, Numerical identification of constitutive parameters in reduced-order bi-dimensional models for pantographic structures: application to out-of-plane buckling, Archive of Applied Mechanics 89 (2019) 1333–1358.

[37] N. Nejadsadeghi, M. De Angelo, R. Drobnicki, T. Lekszycki, F. dell'Isola, A. Misra, Parametric experimentation on pantographic unit cells reveals local extremum configuration, Experimental Mechanics 59 (2019) 927–939.

[38] A. Ciallella, Research perspective on multiphysics and multiscale materials: a paradigmatic case, Continuum Mechanics and Thermodynamics 32 (2020) 527–539.

[39] C. A. Tran, M. Gołaszewski, E. Barchiesi, Symmetric-in-plane compression of polyamide pantographic fabrics—modelling, experiments and numerical exploration, Symmetry 12 (2020) 693.

[40] M. Spagnuolo, M. E. Yildizdag, U. Andreaus, A. M. Cazzani, Are higher-gradient models also capable of predicting mechanical behavior in the case of wide-knit pantographic structures?, Mathematics and Mechanics of Solids 26 (2021) 18–29.

[41] N. Nejadsadeghi, M. Laudato, M. De Angelo, A. Misra, Mechanical Behavior Investigation of 3D Printed Pantographic Unit Cells via Tension and Compression Tests, in: Developments and Novel Approaches in Biomechanics and Metamaterials, Springer, 2020, pp. 409–422.

[42] V. A. Eremeyev, C. Boutin, D. Steigmann, et al., Linear pantographic sheets: existence and uniqueness of weak solutions, Journal of Elasticity 132 (2018) 175–196.

[43] V. A. Eremeyev, F. S. Alzahrani, A. Cazzani, T. Hayat, E. Turco, V. Konopińska-Zmysłowska, et al., On existence and uniqueness of weak solutions for linear pantographic beam lattices models, Continuum Mechanics and Thermodynamics 31 (2019) 1843–1861.

[44] A. Misra, P. Poorsolhjouy, Identification of higher-order elastic constants for grain assemblies

based upon granular micromechanics, Mathematics and Mechanics of Complex Systems 3 (2015) 285–308.

[45] L. Placidi, U. Andreaus, A. Della Corte, T. Lekszycki, Gedanken experiments for the determination of two-dimensional linear second gradient elasticity coefficients, Zeitschrift für angewandte Mathematik und Physik 66 (2015) 3699–3725.

[46] L. Placidi, L. Greco, S. Bucci, E. Turco, N. L. Rizzi, A second gradient formulation for a 2D fabric sheet with inextensible fibres, Zeitschrift für angewandte Mathematik und Physik 67 (2016) 1–24.

[47] Y. Rahali, I. Goda, J.-F. Ganghoffer, Numerical identification of classical and nonclassical moduli of 3D woven textiles and analysis of scale effects, Composite structures 135 (2016) 122–139.

[48] G. Rosi, L. Placidi, N. Auffray, On the validity range of strain-gradient elasticity: a mixed static-dynamic identification procedure, European Journal of Mechanics-A/Solids 69 (2018) 179–191.

[49] H. Yang, B. E. Abali, D. Timofeev, W. H. Müller, Determination of metamaterial parameters by means of a homogenization approach based on asymptotic analysis, Continuum Mechanics and Thermodynamics (2019) 1–20.

[50] M. De Angelo, L. Placidi, N. Nejadsadeghi, A. Misra, Non-standard Timoshenko beam model for chiral metamaterial: Identification of stiffness parameters, Mechanics Research Communications 103 (2020) 103462.

[51] L. Greco, An iso-parametric G^1-conforming finite element for the nonlinear analysis of Kirchhoff rod. Part I: the 2D case, Continuum Mechanics and Thermodynamics 32 (2020) 1473–1496.

[52] I. Giorgio, A. Ciallella, D. Scerrato, A study about the impact of the topological arrangement of fibers on fiber-reinforced composites: some guidelines aiming at the development of new ultra-stiff and ultra-soft metamaterials, International Journal of Solids and Structures 203 (2020) 73–83.

[53] I. Giorgio, A discrete formulation of kirchhoff rods in large-motion dynamics, Mathematics and Mechanics of Solids 25 (2020) 1081–1100.

[54] M. A. Sutton, J. J. Orteu, H. Schreier, Image correlation for shape, motion and deformation measurements: basic concepts, theory and applications, Springer Science & Business Media, 2009.

[55] F. Hild, S. Roux, Digital Image Correlation, in: P. Rastogi, E. Hack (Eds.), Optical Methods for Solid Mechanics. A Full-Field Approach, Wiley-VCH, Weinheim (Germany), 2012, pp. 183–228.

[56] M. A. Sutton, Computer vision-based, noncontacting deformation measurements in mechanics: a generational transformation, Applied Mechanics Reviews 65 (2013).

[57] M. E. Yildizdag, C. A. Tran, E. Barchiesi, M. Spagnuolo, F. dell'Isola, F. Hild, A multi-disciplinary approach for mechanical metamaterial synthesis: A hierarchical modular multiscale cellular structure paradigm, in: State of the Art and Future Trends in Material Modeling, Springer, 2019, pp. 485–505.

[58] E. Turco, A. Misra, M. Pawlikowski, F. dell'Isola, F. Hild, Enhanced Piola–Hencky discrete models for pantographic sheets with pivots without deformation energy: numerics and experiments, International Journal of Solids and Structures 147 (2018) 94–109.

[59] F. Hild, A. Misra, et al., Multiscale DIC applied to pantographic structures, Experimental Mechanics 61 (2021) 431–443.

[60] N. Nejadsadeghi, M. De Angelo, A. Misra, F. Hild, Multiscalar DIC analyses of granular string under stretch reveal non-standard deformation mechanisms, International Journal of Solids and Structures (2022) 111402.

[61] E. Turco, A. Misra, R. Sarikaya, T. Lekszycki, Quantitative analysis of deformation mechanisms in pantographic substructures: experiments and modeling, Continuum Mechanics and Thermodynamics 31 (2019) 209–223.

[62] A. Tikhonov, V. Arsenin, Solutions of ill-posed problems, J. Wiley, New York (USA), 1977.

[63] Z. Tomičević, F. Hild, S. Roux, Mechanics-aided digital image correlation, The Journal of Strain Analysis for Engineering Design 48 (2013) 330–343.

[64] J. Neggers, F. Mathieu, F. Hild, S. Roux, Simultaneous full-field multi-experiment identification, Mechanics of Materials 133 (2019) 71–84.

[65] M. E. Yildizdag, E. Barchiesi, F. dell'Isola, Three-point bending test of pantographic blocks: numerical and experimental investigation, Mathematics and Mechanics of Solids 25 (2020) 1965–1978.